3-D modeling of stresses and strains in accessory carpal bone under maximum compressive loading

T. Reuter[1], J. Gernhardt[2], C. Rutter[1], C. Lischer[2]

1. Industrial Engineering, Institut Chemnitzer Maschinen- und Anlagenbau e.V., Chemnitz, Germany.
2. Equine Clinic: Surgery and Radiology, Freie Universität Berlin, Berlin, Germany.

Abstract

When treating fractures of the accessory carpal bones in horses, it is important to understand the forces that implants (screws and plates) must withstand. The etiology of the fracture is not fully understood, but their high incidence during exercise suggests a relation to biomechanical forces. Detailed descriptions of the intact and fractured accessory carpal bone's morphology and functional anatomy, which are crucial for stable fracture fixation, are lacking. Therefore, the aim of this study is to create a 3D FEM model for simulating the optimal selection and placement of implants. The primary focus of this work is to create and validate the model through an FEM study in order to calculate the stresses and strains that occur in the accessory carpal bone under maximum compression (force-to-failure) at different Young's moduli (E = 4 GPa – 30 GPa). The maximum strength was performed on accessory carpal bones of horses (n = 8) by experimental compression tests. A 3D FEM model was then created in COMSOL® Multiphysics using the Nonlinear Structural Materials Module. The morphology of the bone was obtained from CT scans. Boundary conditions were derived from the experimental uniaxial compression test. The results from the compression tests revealed averaged force-to-failure values of F_{mean} = 11.46 +/- 2.49 kN. The calculated stresses ranged from σ = 500 – 3000 MPa, depending on the Young's modulus used. The simulated deformations behavior matched those obtained from the experimental compression tests. Thus, the comparison of the simulated deformations with those from the experimental tests helped narrow down the Young's modulus range (E = 4 GPa – 6 GPa). The simple 3D FEM model developed in this study can be used for initial investigations to understand the etiology of the fracture and for the selection and placement of implants for stable fracture fixation of the accessory carpal bone.

Keywords: Accessory Carpal Bone (ACB), FEM, Maximum Compressive Loading, Neo-Hookean, CT-Scan, 3D-Modeling, Force-to-Failure.

Introduction

The accessory carpal bone (ACB) is one of seven bones of the carpal joints of the horse. It has a discoid shape, the outer (lateral) surface is convex and the inner (medial) surface is concave. In the carpus of the horse, the ACB is connected with two muscles and several ligaments, although it has no weight-bearing function [1]. Fractures of the bone are rarely seen but mostly occur in racehorses and other equine athletes [2, 3]. The ACB is usually fracturing in a vertical plane [4, 5]. Less commonly, it is breaking horizontally [6]. Conservative treatment with bandaging and box rest is usually chosen, which can lead to bony non-union and severe callus formation. Therefore, surgical treatment is sought, which is technically difficult due to the shape of the bone [7]. Combined with the low incidence of the fracture, which is about 2% of all carpal bone fractures [8, 9, 10] the decision for treatment management is difficult [3]. By loading the bone under maximum compression (force-to-failure), the authors aimed to demonstrate the maximum strength of the bone, which is important to ensure stable fracture fixation in the living horse. In addition, there has been no previous study in which the fracture was artificially induced by compression to determine whether the fracture behavior of the artificial compression fracture is comparable to the natural fracture of the horse.

Therefore, the aim of this study is to create a 3D FEM model for simulating the optimal selection and placement of implants. The primary focus of this work is to create and validate the model through an FEM study in order to calculate the stresses and strains that occur in the ACB under maximum compression (force-to-failure) at different Young's moduli. The paper is organized as follows: First, an overview of the main functions of bone tissue is given with their corresponding biomechanical properties as well as the associated material models. Next, the experimental procedure and the numerical model with the corresponding equations are explained. Then, the experimental and simulation results are presented. Finally, a discussion is derived followed by conclusion and outlook.

Theory

Bones are the essential prerequisite for higher organisms to have a defined shape. Combined with muscles and tendons, they enable locomotion and stability as well as other motor activities. In addition, they have a protective function. There are different types of bones: long, short, flat as well as irregular. Bones are strongly structured in order to be able to fulfill their various tasks optimally [11]. They must be able to absorb different forces, which can take the form of stretching, compression, bending, torsion or shearing, and must be adapted

accordingly to all these loads [12, 13]. The special properties of bones include: strong mineralization, high adaptability to loads (increased bone formation due to mechanical stimuli) and the ability to absorb and redirect forces at low weight [11, 13]. Due to the complex structure of bones, in particular because of the anisotropy of the mechanical properties as well as the influence of temperature, mineralization state, bone type, strain rate and time, there are a large number of different complex material models (linear elastic, transversely isotropic, poroelastic, viscoelastic) in the literature for describing bone behavior in response to different loading scenarios [14, 15, 16, 17]. With an increase in complexity, more and more parameters are required, which means an additional experimental effort. Biomechanical characterization of ACB was mainly performed using bone mineral density [18]. Therefore, the magnitudes of the biomechanical properties from the human domain will be used here. The Young's modulus of human cortical bone varies between 6.91 GPa and 21 GPa (longitudinal direction) as well as 5 GPa and 13 GPa (transverse direction). Poisson's ratio ranges from 0.12 to 0.58. Compressive strength ranges from 70 to 280 MPa (longitudinal direction) and about 50 MPa (transverse direction) [12, 14, 19, 20].

Experimental Set Up
Eight ACB from slaughtered warmblood horses (age 13 – 18 years) were collected. Sex, race, and size of the horses were unknown. Visual inspection revealed no damage to the ACB. The ACB were then stripped of all soft tissue remains and stored at -24 °C. Twelve hours before examination, the ACB were thawed at room temperature. The shape (outer surface and top view) of the ACB is shown in Figure 1.
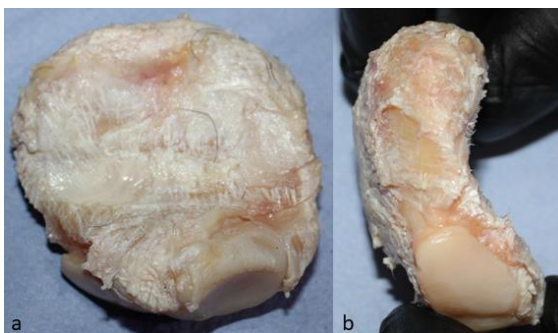

Figure 1. Accessory carpal bone specimen: a.) outer surface view and b.) top view.

The maximum strength (force-to-failure) of the ACB was determined by quasi-static uniaxial compression tests using a four-column testing machine. Special fixtures were designed for clamping the ACB, which were adapted to the top and bottom of the ACB (specimen holder). The following scheme was defined for the execution of the tests: 1. the specimens were preconditioned

(five times compression loading up to F = 2 kN with a test velocity v_1 = 100 N/s); 2. conducting the compressive tests until the specimens were damaged with a test velocity v_2 = 1 mm/s. The experimental setup is shown in Figure 2.
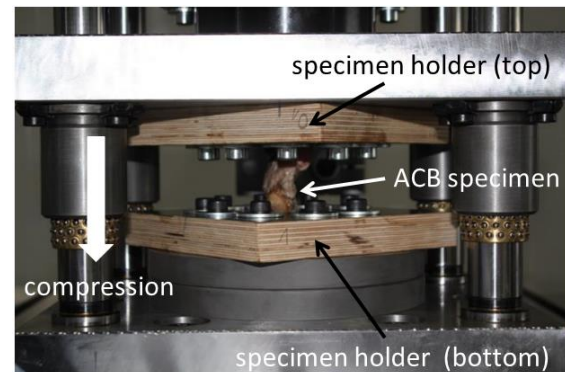

Figure 2. Experimental setup to determine the maximum strength (force-to-failure) of the accessory carpal bone.

The obtained data were statistically analyzed using the boxplot. After the experiments, the damage to the ACB was determined visually.

Numerical Model
To calculate the stresses and strains in the ACB at maximum compression, a 3D FEM model was created in COMSOL® Multiphysics using the Structural Mechanics Module, the Nonlinear Structural Materials Module, and the CAD Import Module. The 3D spatial dimension, the Solid Mechanics (solid) physics interface, and the steady-state study were selected as the modeling basis. The following steps were taken to build the 3D FEM model: Firstly, CT scans of the bone were taken. In step 2, CT scans were used to convert the ACB morphology into a step file (3D slicer®), which was then loaded into COMSOL Multiphysics (CAD Import Module). Subsequently, in step 3, the boundary conditions were defined according to the experimental uniaxial compression tests. Surfaces were defined for the bottom and top of the ACB, which corresponded to the dimensions from the specimen holder. A fixed constraint was defined for the ACB bottom and a boundary load (negative x-direction) was defined for the ACB top. The boundary load corresponded to the force-to-failure (mean) from the experimental tests. Figure 3 shows the geometry of the ACB and the boundary conditions for the 3D FEM model. In step 4, a hyperelastic material model according to Neo-Hookean (incompressible) was then selected to describe the material behavior of the bone. The material parameter Young's modulus was varied (see Methods) and the material parameter Poisson's ratio was kept constant at v = 0.4 [14]. The 5th step involved the creation of the FEM mesh. For this purpose, the sequence type physics-controlled mesh was selected with an extra fine element size (element type tetrahedra). The mesh fineness was

2

selected according to a mesh convergence study. The mesh consisted of 82168 elements.
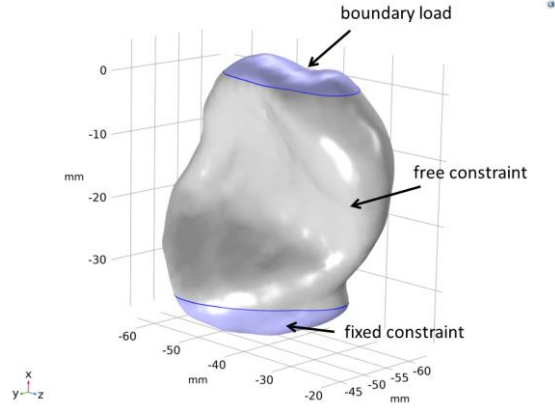

Figure 3. The 3D FEM model with the boundary conditions.

Figure 4 shows the mesh and Figure 5 the mesh quality. The mesh quality with the quality description skewness (a measure of the equiangular skew) ranged from 0.213 to 0.969. The mean mesh quality was 0.660.
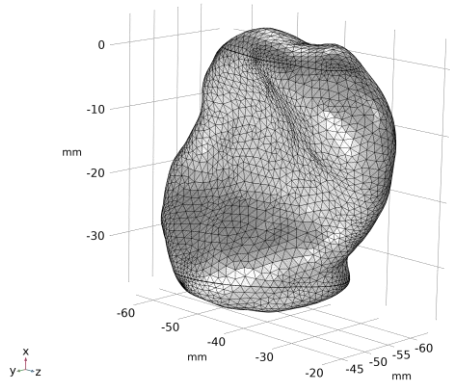

Figure 4. The FEM mesh with extra fine element size.

The last step was to define the solver settings. The PARDISO solver with default settings was used as direct solver. For the calculation, an auxiliary sweep was created with variation of the boundary load and the Young's modulus (see Methods).
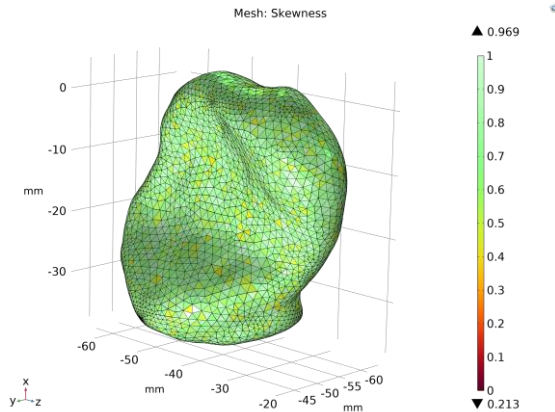

Figure 5. The FEM mesh quality.

The simulations were performed with the HP Z8 G4 workstation (256 GB DDR4 memory, 2x Intel Xeon 6244 3.6 2933 MHz CPU, NVIDIA Quadro RTX 4000 8 GB). In a final step, the stress, strain, and displacement data were evaluated.

Governing Equations

The mathematical description of the 3D FEM model can be divided into two categories: Material model and boundary conditions. The Neo-Hookean incompressible hyperelastic material model was used to describe the ACB. An isotropic hyperelastic material is defined by its elastic strain energy density W_S, which is a function of the elastic strain state. The hyperelastic formulation yields a nonlinear relationship between stress and strain. Strain energy density W_S is described in equation 1:

$$W_S = \frac{1}{2}\mu(\bar{I}_1 - 3). \qquad \text{(Eq. 1)}$$

Here, μ is the Lamé parameter and $\bar{I}_1$ is the first invariant of the elastic right Cauchy–Green deformation tensor C. The conversion of the Lamé constant to Young's modulus is shown in Equation 2.

$$\mu = \frac{1}{2} \cdot \frac{1}{1+\nu} \cdot E. \qquad \text{(Eq. 2)}$$

Here, E is the Young's modulus and ν the Poisson's ratio [21, 22, 23]. After the strain energy density is defined, the second Piola-Kirchhoff stress is calculated as follows:

$$S = 2\frac{\partial W_S}{\partial C}. \qquad \text{(Eq. 3)}$$

For incompressible hyperelastic materials, the volumetric strain energy density W_{vol} is not defined at all, and the strain energy density W_S only consists of the isochoric contribution and the incompressibility constraint (J = 1). Thus, the Cauchy stress tensor can be described by equation 4 and the Green-Lagrange strain tensor by equation 5.

$$\sigma = J^{-1}FSF^T \qquad \text{(Eq. 4)}$$

$$\epsilon = \frac{1}{2}(F^TF - I) \qquad \text{(Eq. 5)}$$

Here, F is the deformation gradient, I is the invariant of the elastic right Cauchy–Green deformation tensor C and J is the volumetric deformation, which can be calculated using Equation 6 [22, 23].

$$J = det(F) \qquad \text{(Eq. 6)}$$

The boundary conditions were defined by using a boundary load and a fixed condition. The boundary load is defined in equations 7 and 8.

$$F_A = S \cdot n \qquad \text{(Eq. 7)}$$

$$F_{tot} = F_A A \qquad \text{(Eq. 8)}$$

For Force per unit area (F_A), the traction components are given explicitly (n is the positive normal direction). To calculate the total force (F_{tot}), F_{tot} is divided by the area A of the boundaries on which the load acts. Then the force is applied in the same way as for the force per unit area. The fixed constraint adds a condition that fixes the geometric element, i.e., the displacements are zero in all directions of the selected geometric elements. If there are rotational degrees of freedom, they are also equal to zero [24].

Methods (Numerical Study)

For the characterization of the ACB under maximum strength (force-to-failure), two numerical studies were conducted. The first numerical study was performed as a function of Young's modulus and boundary load to be able to calculate the stresses, strains, and displacements of the ACB. The Young's modulus varied from E = 4 GPa to 30 GPa in 2 GPa steps and the boundary load from F = 1 kN to 18 kN in 1 kN steps (an auxiliary sweep was performed). The second numerical study included the simulations with the minimum, maximum and average values of the experimental boundary loads. From the second numerical study, the simulated deformations were compared to the experimental deformations to narrow down the Young's modulus range.

Experimental Results

The experimental results from the compression tests revealed averaged values for the force-to-failure of $F_{mean} = 11.46 +/- 2.49$ kN. The minimum and maximum values are $F_{min} = 9.12$ GPa and $F_{max} = 14.50$ GPa, respectively. Figure 6 shows the statistical distribution of the force-to-failure values of the ACB specimens tested.
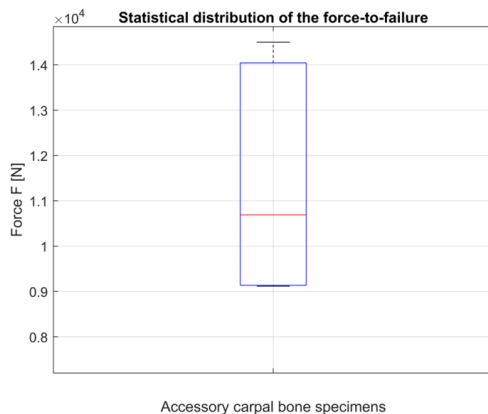

Figure 6. Statistical distribution of force-to-failure values of ACB specimens.

Figure 7 shows the ACB specimen before and after the compression tests. Bone damage typically occurs in a vertical plane between half and two-thirds of the ACB and in the area where the ACB is clamped in the testing machine.
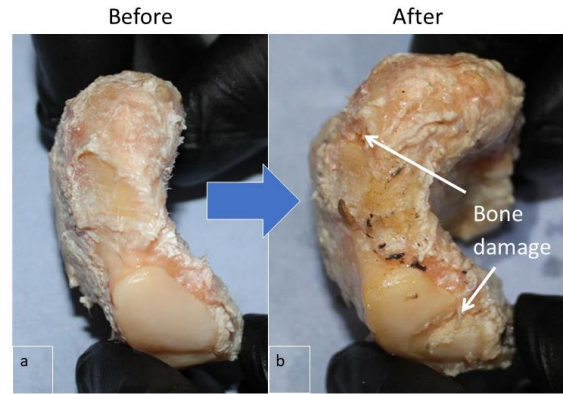

Figure 7. Accessory carpal bone specimen: a.) Before and b.) after compression test.

Simulation Results

The results from the first numerical study showed that the calculated maximum stresses ranged from σ = 500 to 3000 MPa and maximum strains ranged from ε = 0.001 to 0.4 depending on the Young's modulus and boundary load. Figures 8 and 9 show the calculated maximum stresses and strains as a function of Young's modulus and boundary load. In addition, the experimental boundary loads (minimum and maximum) have been plotted in the figures.
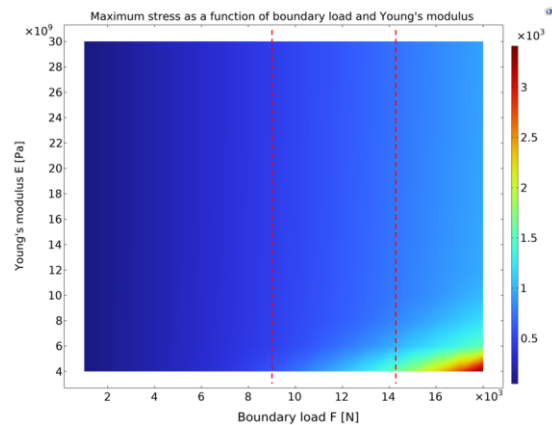

Figure 8. Calculated maximum stresses as a function of boundary load and Young's modulus (red lines - minimum and maximum of experimental boundary load).
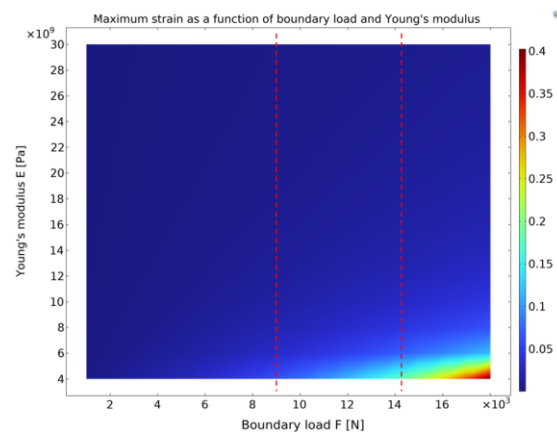

Figure 9. Calculated maximum strains as a function of boundary load and Young's modulus (red lines - minimum and maximum of experimental boundary load).

The second numerical study showed that the simulated deformation behavior complied well with the results obtained from the experimental compression tests. At a boundary load of F_{mean} = 11.46 kN, good compliance was found between simulated and experimental deformation behavior at a Young's modulus of E = 5 GPa. After the analysis of the second numerical study, the Young's modulus range can be narrowed down to 4 and 6 GPa. Figure 10 shows the comparison between simulated and experimental deformation behavior. The analysis of the calculated stresses showed that the highest stresses occurred both in the bone fracture, typically in a vertical plane between half and two-thirds of the bone, and in the area where the bone was clamped in the testing machine. Figure 11 shows the stress analysis of the ACB after compression test.
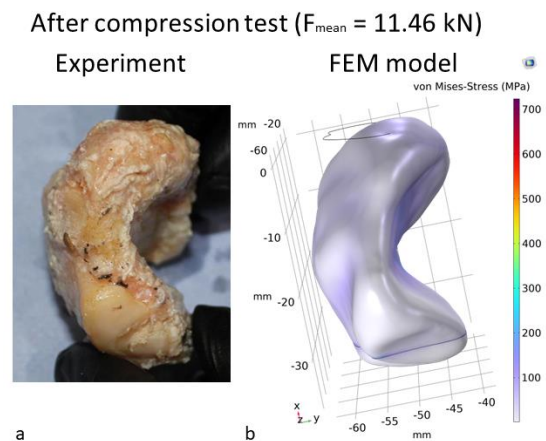

Figure 10. Comparison between simulated and experimental deformation behavior: a.) Experiment and b.) 3D FEM model (E = 5 GPa).

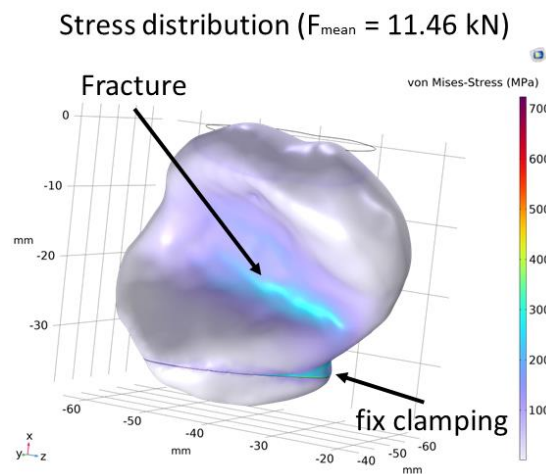*Figure 11. Simulated stress distribution of the ACB under compression (E = 5 GPa).*

The calculated stresses in the fracture area are between σ = 150 MPa and σ = 250 MPa. The maximum stresses occurred at the specimen clamping. The results of the simulated stresses and strains from the second numerical study are presented in the appendix.

Discussion

The experimental compression tests on equine ACB resulted in fracture patterns similar to those of natural fracture behavior in horses [4, 5, 6]. The variability of the force-to-failure values obtained is within the typical range for the study of biological materials. However, the variance may be caused by limitation in the experimental setup, such as specimen movement during the compression tests as well as minor pre-damage of the specimens during preconditioning. Nevertheless, the obtained values can be used for the numerical study. The results of the numerical studies show that the stress and strain characteristics calculated with the simple 3D FEM model strongly depend on the material properties (Young's modulus) and load conditions. The bone deformations obtained from the experimental compression tests are consistent with the simulated deformation behaviors. Thus, comparison of the simulated deformations with those from the experimental tests helps to narrow down the range of Young's modulus greatly from E = 30 GPa to a maximum of E = 6 GPa. These values comply well with typical Young's modulus data from the literature [14, 19]. The obtained Young's modulus range is only applicable to the simple 3D FEM model, since this is an isotropic model [15]. The stresses calculated from this 3D FEM model occur both in the region of experimental bone fracture, typically in a vertical plane between half and two-thirds of the bone, and in the region where the bone was fixed in the testing machine. The simulated maximum stress ranges comply very well with the maximum bone damage that occur in the ACB after the compression tests. After validation of the 3D FEM model, simple fracture characterizations (etiology of the fracture) and initial model calculations for the selection and placement of implants for stable fixation of fractures of the ACB can thus be performed. A detailed description of the fracture characteristics with different force vectors can only be performed to a limited extent with this 3D FEM model, since the anisotropy of the material properties of bone was not considered [14, 15].

Conclusions and Outlook

There are several theories of the suspected etiology of the fracture of the ACB but until now the biomechanical development of it is not fully understood. The simple 3D FEM model developed in this study can be used for initial investigations into understanding the etiology of the fracture and for the selection and placement of implants for stable fracture fixation of the ACB. The Young's modulus values determined here can be used as initial guide values for the simple simulation model. Future work will focus on improving the 3D FEM model. This includes determining the material properties of the bone (inverse FEM [25] or experimental) and employing more complex

material models. Likewise, fracture formation can be simulated, which is not considered in this 3D FEM model.

References

[1] S. Sisson, "Bones of the Thoracic Limb," in *The Anatomy of the Domestic Animals*, Philadelphia and London, Saunders Company, 1917, pp. 93-98.

[2] C. Kawcak, "The Carpus," in *Adams and Stashak's Lameness in Horses*, Hoboken, NJ, Wiley-Blackwell, 2020, pp. 597-619.

[3] A. Ruggles, "Carpus," in *Equine Surgery*, St. Louis, MO, Elsevier, 2019, pp. 1658-1660.

[4] C. McIlwraith, "Fractures of the Carpus," in *Equine Fracture Repair*, Hoboken, NJ, Wiley-Blackwell, 2020, pp. 480-514.

[5] G. Minshall, "Frontal Plane Fractures of the Accessory Carpal Bone and Implications for the Carpal Sheath of the Digital Flexor Tendons," *Equine Veterinary Journal*, pp. 579-584, 2014.

[6] D. Carson, "Horizontal Fracture of the Accessory Carpal Bone in a Thoroughbred Racehorse," *Veterinary Education*, pp. 173-176, 1990.

[7] T. Launois, "Accessory Carpal Bone Fixation in Cases of Simple Frontal Fracture, using the dorso 80° proximo 30° lateral - palmarodistomedial (Skyline) View," in *Proceedings of the European College of Veterinary Surgeons, 10th Annual Scientific Meeting*, Velbert, Germany, 2001.

[8] R. Wyburn, "Fractures of the Equine Carpus: A Report on 57 Cases," *Veterinary Surgery*, pp. 133-142, 1974.

[9] D. Thrall, "Five-Year Survey of the Incidence and Location of Equine Carpal Chip Fractures," *Journal of the American Veterinary Medical Association*, 1970.

[10] A. Barr, "Fractures of the Accessory Carpal Bone in the Horse," *Veterinary Record*, pp. 432-434, 1990.

[11] M. Schünke and A. Faller, Der Körper des Menschen, Stuttgart: Georg Thieme Verlag KG, 2016.

[12] E. Morgan, G. Unnikrisnan and A. Hussein, "Bone Mechanical Properties in Healthy and Diseased States," *Annual Review of Biomedical Engineering*, vol. 20, pp. 119-143, 2018.

[13] W. Lohmann, H. Markl and H. Ziegler, Biophysik - Ein Lehrbuch, Berlin Heidelberg New York: Springer-Verlag, 1982.

[14] S. Cowin and S. Doty, Tissue Mechanics, New York: Spriner Science+Business Media, 2007.

[15] D. Pahr and A. Reisinger, "A Review on Recent Advances in the Constitutive Modeling of Bone," *Current Osteoporosis Reports*, vol. 18, pp. 696-704, 2020.

[16] M. Hoffmann, T. Reuter, M. Lange and F. Meuche, "A elastic and a hyper elastic model of cartilage - the simulation in comparison with the experiment," *Biomedical Engineering*, vol. 55, pp. 6-9, 2010.

[17] T. Reuter and I. Ponomarev, "Biomechanical parameter determination of scaffold-free cartilage constructs (SFCCs) with the hyperelastic material models Yeoh, Ogden and Demiray," *Current Directions in Biomedical Engineering*, vol. 1, no. 1, pp. 442-445, 2015.

[18] L. Vulcano and F. Santos, "Determination and Padronization of Normal Values of Bone Mineral Density (BMD) of the Acessory Carpus Bone in Young Thoroughbred Horse using Opticaldensitometry in Radiographic Image," *Brazilian Journal of Veterinary Research and Animal Science*, vol. 40, pp. 54-61, 2003.

[19] J. Vinvent, Structural Biomaterials, New Jersey: Princeton University Press, 1990.

[20] R. Oftadeh, M. Perez-Viloria, J. Villa-Camacho, A. Vaziri and A. Nazarian, "Biomechanics and Mechanobiology of Trabecular Bone: A Review," *Journal of Biomechanical Engineering*, vol. 137, no. 1, p. 010802, 2015.

[21] G. Mavko, T. Mukerji and J. Dvorkin, The Rock Physics Handbook., Cambridge: Cambridge University Press, 2003.

[22] W. Slaughter, The Linearized Theory of Elasticity, New York: Spriner Science+Business Media, 2002.

[23] A. Boresi, R. Schmidt and O. Sidebottom, Advanced Mechanics of Materials, New York: John Wiley & Sohns, 1993.

[24] COSMOL, Structural Mechanics Theory, Göttingen: COMSOL, 2023.

[25] T. Reuter and C. Hurschler, "Biphasic parameter identification of equine articular cartilage from creep indentation data using an optimized 3D FE-based method," *Current Directions in Biomedical Engineering*, vol. 4, no. 1, pp. 481-484, 2018.

Appendix

The following figures present the results of the second numerical study. Figures 12 to 17 show the stress and strain results for F_{min}, F_{mean} and F_{max}.
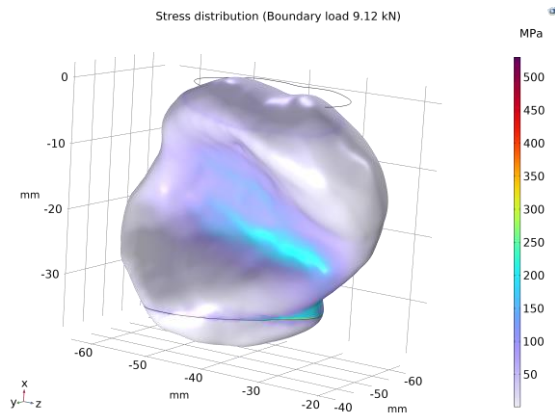

Figure 12. Simulated stress distribution of the ACB under compression (F_{min} = 9.12 kN, E = 5 GPa).
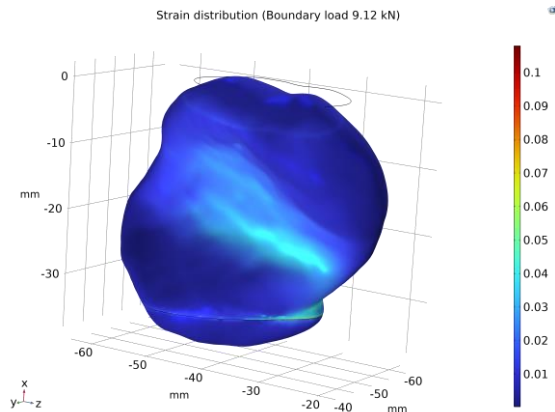

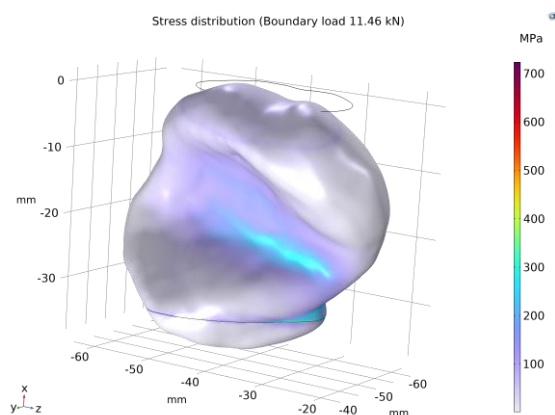*Figure 13. Simulated strain distribution of the ACB under compression (F_{min} = 9.12 kN, E = 5 GPa).*

Figure 14. Simulated stress distribution of the ACB under compression (F_{mean} = 11.46 kN, E = 5 GPa).
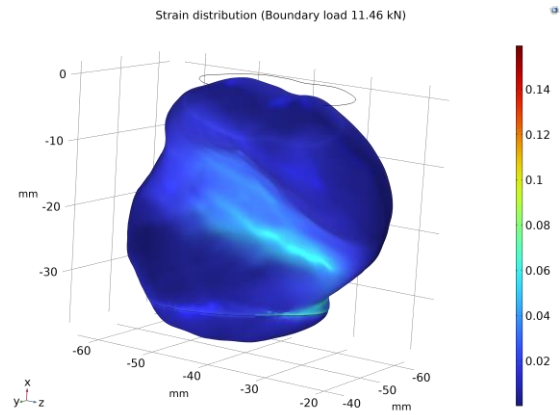

Figure 15. Simulated strain distribution of the ACB under compression (F_{mean} = 11.46 kN, E = 5 GPa).
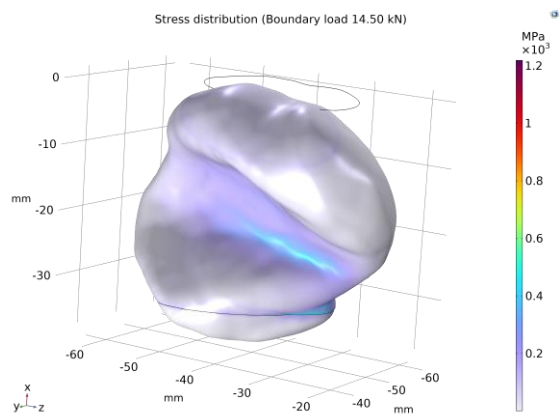

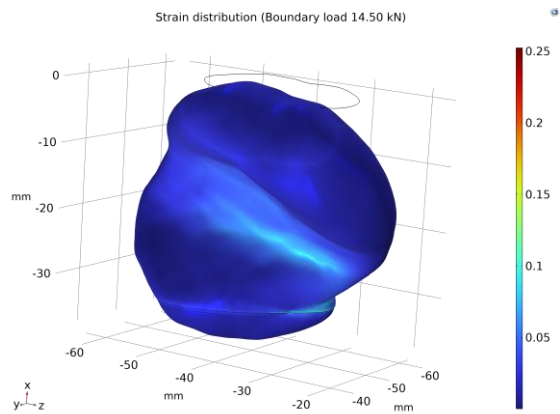*Figure 16. Simulated stress distribution of the ACB under compression (F_{max} = 14.50 kN, E = 5 GPa).*

Figure 17. Simulated strain distribution of the ACB under compression (F_{max} = 14.50 kN, E = 5 GPa).